

RESEARCH ARTICLE

10.1002/2014JB011548

Key Points:

- We find low-velocity zones along the SJFZ using a new data set
- The low-velocity zones have along-strike variations along the SJFZ
- The damage zone at Anza indicates slow healing process

Supporting Information:

- Readme
- Table S1
- Table S2

Correspondence to:

H. Yang,
hyang@cuhk.edu.hk

Citation:

Yang, H., Z. Li, Z. Peng, Y. Ben-Zion, and F. Vernon (2014), Low-velocity zones along the San Jacinto Fault, Southern California, from body waves recorded in dense linear arrays, *J. Geophys. Res. Solid Earth*, 119, 8976–8990, doi:10.1002/2014JB011548.

Received 19 AUG 2014

Accepted 17 NOV 2014

Accepted article online 25 NOV 2014

Published online 17 DEC 2014

Low-velocity zones along the San Jacinto Fault, Southern California, from body waves recorded in dense linear arrays

Hongfeng Yang¹, Zefeng Li², Zhigang Peng², Yehuda Ben-Zion³, and Frank Vernon⁴

¹Earth System Science Programme, Faculty of Science, Chinese University of Hong Kong, Shatin, Hong Kong, ²School of Earth and Atmospheric Sciences, Georgia Institute of Technology, Atlanta, Georgia, USA, ³Department of Earth Sciences, University of Southern California, Los Angeles, California, USA, ⁴Scripps Institution of Oceanography, University of California, San Diego, La Jolla, California, USA

Abstract We derive high-resolution information on low-velocity fault zone (FZ) structures along the San Jacinto Fault Zone (SJFZ), Southern California, using waveforms of local earthquakes that are recorded at multiple linear cross-fault arrays. We observe clear across-fault delays of direct *P* and *S* waves, indicating damage zones at different segments of the SJFZ. We then compute synthetic traveltimes and waveforms using generalized ray theory and perform forward modeling to constrain the FZ parameters. At the southern section near the trifurcation area, the low-velocity zone (LVZ) of the Clark branch has a width of ~200 m, 30–45% reduction in *V_p*, and ~50% reduction in *V_s*. From array data across the Anza seismic gap, we find a LVZ with ~200 m width and ~50% reduction in both *V_p* and *V_s*, nearly as prominent as that on the southern section. We only find prominent LVZs beneath three out of the five arrays, indicating along-strike variations of the fault damage. FZ-reflected phases are considerably less clear than those observed above the rupture zone of the 1992 Landers earthquake shortly after the event. This may reflect partially healed LVZs with less sharp boundaries at the SJFZ, given the relatively long lapse time from the last large surface-rupturing event. Alternatively, the lack of observed FZ-reflected phases could be partially due to the relatively small aperture of the arrays. Nevertheless, the clear signatures of damage zones at Anza and other locations indicate very slow healing process, at least in the top few kilometers of the crust.

1. Introduction

Crustal faults are generally associated with damage zones that have intensive fractures around the main slip surface [e.g., Chester *et al.*, 1993; Ben-Zion and Sammis, 2003]. The damage zones are characterized by lower elastic moduli and seismic velocities compared to the host rocks. They reflect the behavior of past earthquakes [e.g., Dor *et al.*, 2006; Ben-Zion and Ampuero, 2009; Xu *et al.*, 2012] and can exert significant influence on properties of future ruptures [e.g., Harris and Day, 1997; Ben-Zion and Huang, 2002; Huang *et al.*, 2014], amplification of ground motion near faults [e.g., Wu *et al.*, 2009; Avallone *et al.*, 2014; Kurzon *et al.*, 2014], and long-term deformation processes [e.g., Finzi *et al.*, 2009; Kaneko *et al.*, 2011]. A detailed high-resolution imaging of fault zone (FZ) structure can therefore provide important constraints on the behavior of past and future earthquakes on the fault.

A number of investigations have been conducted to probe FZ properties. These include direct geological mapping and analysis of FZ samples [e.g., Chester *et al.*, 1993; Wechsler *et al.*, 2009; Li *et al.*, 2013], modeling fracture densities [e.g., Schulz and Evans, 1998; Smith *et al.*, 2013], modeling geodetic observations [e.g., Fialko *et al.*, 2002; Lindsey *et al.*, 2014], examining high-resolution earthquake locations [e.g., Schaff *et al.*, 2002; Yang *et al.*, 2009; Valoroso *et al.*, 2014], performing local earthquake and ambient noise tomography [e.g., Thurber *et al.*, 2006; Allam and Ben-Zion, 2012; Zhang and Gerstoft, 2014; Zigone *et al.*, 2014a], and modeling a variety of FZ-related seismic phases [e.g., Li *et al.*, 1990; Ben-Zion *et al.*, 2003; Li *et al.*, 2007; Hillers *et al.*, 2014]. So far, the highest imaging resolution of fault damage zones is obtained from modeling high-frequency waveforms recorded at small-aperture arrays across the FZ [e.g., Ben-Zion and Sammis, 2003].

Using dense FZ arrays, several studies attempted to image detailed FZ structures along the San Jacinto Fault Zone (SJFZ) in Southern California. A common feature of their results is the existence of a low-velocity

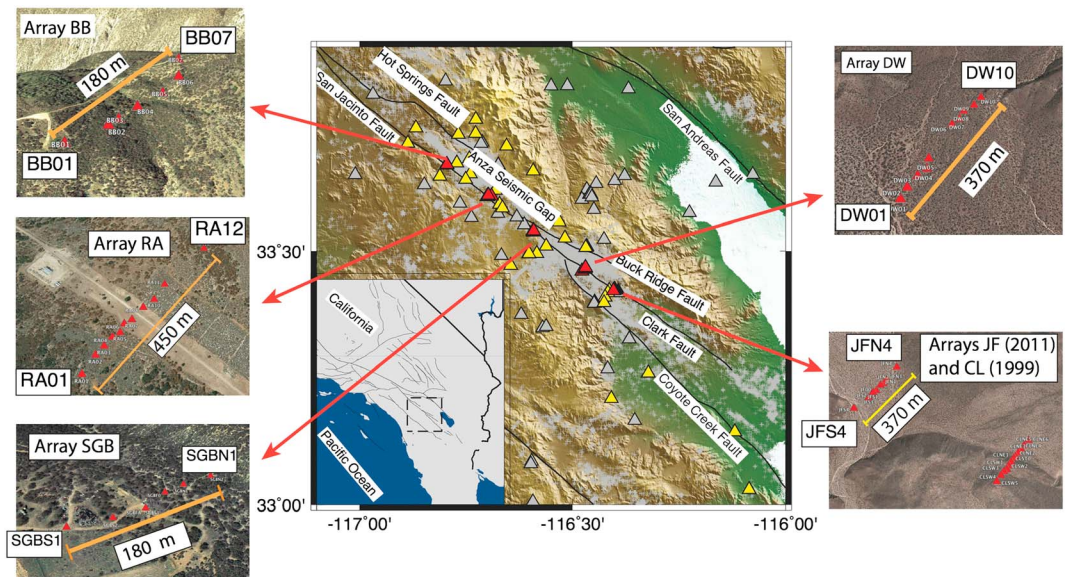


Figure 1. Map showing the San Jacinto Fault and faults (black lines), and seismicity since 1981 (grey crosses). Triangles represent seismic stations in the region, including the recent deployment since 2010 (yellow and red). Red triangles show locations of five small-aperture arrays across the fault, and a zoom-in plot for each array is plotted on top of the Google map. The inset marks the location of the study region in California.

zone (LVZ) of 75–150 m in width with 25%–50% reduction in V_p and V_s [e.g., *Li et al.*, 1997; *Li and Vernon*, 2001; *Lewis et al.*, 2005; *Yang and Zhu*, 2010]. The depth extent of the LVZ remains a subject of debate. Based on analysis of FZ-trapped waves recorded by several cross-fault arrays, *Li et al.* [1997] and *Li and Vernon* [2001] suggested that a 15–20 km deep LVZ exists along several strands of the SJFZ. Using the same trapped wave data set, however, *Lewis et al.* [2005] argued that the LVZs extend no more than 5 km deep. *Yang and Zhu* [2010] reached the same conclusion by modeling the high-frequency body waves recorded by the same arrays.

In this work we perform high-resolution imaging of FZ properties along several different segments of the SJFZ, using five newly deployed small-aperture arrays (Figure 1). We estimate the FZ dip by analyzing differential traveltimes of P waves across the FZ [*Yang and Zhu*, 2010]. We then determine the internal properties of the FZ structures by analyzing P and S body waves that propagate through and are reflected from the boundaries of the LVZ [*Li et al.*, 2007]. This method can reduce the trade-off between the width and velocity of the LVZ, as shown in previous studies along the Landers and the Calico faults [*Li et al.*, 2007; *Yang et al.*, 2011]. However, the short aperture of the arrays used in this work limits our ability to reduce model trade-offs and also provide strong constraints on the depth extent of the LVZs. The obtained results on the internal structures of the SJFZ at the various positions augment recent detailed tomographic imaging of the SJFZ area [*Allam and Ben-Zion*, 2012; *Allam et al.*, 2014; *Zigone et al.*, 2014a].

2. Tectonic Setting and Data

The SJFZ accommodates a significant portion of the relative motion between the Pacific and North American plates in Southern California. Based on dating-displaced sedimentary deposits and landforms over three distinct time intervals since ~ 700 ka, *Blisniuk et al.* [2013] estimated the slip rate of the SJFZ to be ~ 12 mm/yr, nearly stable since its inception at ~ 1.0 – 1.1 Ma [*Lutz et al.*, 2006]. The slip rate might not be homogeneous along the entire SJFZ. For instance, the southern portion of the SJFZ has been suggested to experience higher slip rate of ~ 19 – 21 mm/yr according to analysis of interferometric synthetic aperture radar data [*Fialko*, 2006]. Owing to the accumulated tectonic strain, numerous microsize to moderate-size earthquakes occur along the SJFZ, making it the most active strand of the San Andreas fault system in Southern California (Figure 1). Since 1890, a series of moderate earthquakes with magnitude larger than 6 have occurred along the fault [*Sykes and Nishenko*, 1984; *Sanders and Kanamori*, 1984]. Paleoseismic investigations near the

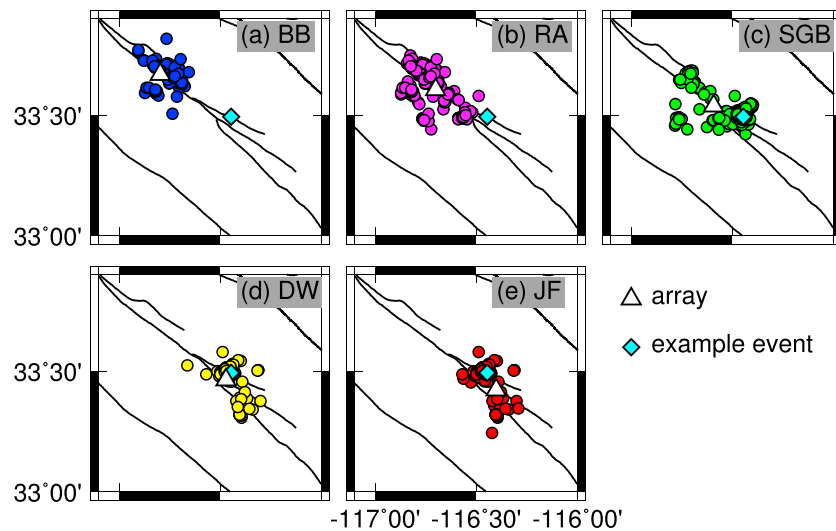


Figure 2. Locations of the five arrays (triangles) and earthquakes used in this study. Colors represent events recorded at the corresponding arrays. Blue diamond: an example M_l 3.4 earthquake on 24 March 2013 recorded at multiple arrays.

Anza seismic gap, the segment between the Hot Springs Fault and the trifurcation area (Figure 1), revealed a series of prehistoric large earthquakes in the past 3500 years, with an average slip of ~ 4 m [Rockwell and Ben-Zion, 2007]. According to an analysis of light detection and ranging (lidar) and field observations, the Anza seismic gap has not ruptured since 1800 [Salisbury *et al.*, 2012].

To better understand the coupled evolution of earthquakes and faults, a dense seismic network has been deployed around the SJFZ since 2010, complementing the coverage of existing permanent stations in the region [e.g., Allam *et al.*, 2014; Kurzon *et al.*, 2014]. The new network includes five small-aperture linear arrays across the different segments of the SJFZ. From northwest to southeast, these are named as BB, RA, SGB, DW, and JF (Figure 1). All these profiles are approximately perpendicular to the surface trace of the fault and range from ~ 180 m to ~ 450 m in length. Additional information about each array, such as operation time, number of stations, and array lengths, can be found in Table S1 in the supporting information. Since the initial deployment, numerous local earthquakes have been recorded at these arrays.

3. Data Analysis and Results

For each small-aperture array, we select local earthquakes with epicentral distances less than 20 km since the initial deployment of that array (Figure 2), based on the standard earthquake locations from the Southern California Earthquake Data Center between January 2012 and April 2013. Table S1 lists the start and end dates of our used catalogs, as well as the cutoff magnitudes for events recorded at each array. We remove instrument responses to obtain velocity waveforms and apply a two-pass Butterworth band-pass filter between 1 and 20 Hz. We then manually pick P and S wave arrivals for each local earthquake and discard the low-quality waveforms with no clear P and/or S waves. We end up with 93, 215, 276, 94, and 98 events for arrays BB, RA, SGB, DW, and JF, respectively (Table S1). Note that some events are recorded by more than one array simultaneously (Figure 2).

3.1. Traveltime Delays of Direct P Waves

We first inspect P wave arrival time delays across each small-aperture array, i.e., traveltime differences between the northeasternmost and southwesternmost stations of the arrays. Such across-array arrival time delays reflect geometrical effects of the array and heterogeneous velocity structure beneath each array. For example, an M_l 3.4 earthquake (the Southern California Earthquake Center (SCEC) catalog ID: 11273498) occurred on 27 March 2013 and was recorded at all the arrays. This event has a catalog depth of 8.5 km and is located on or very close to the Buck Ridge Fault. P waves of this earthquake arrive nearly the same time

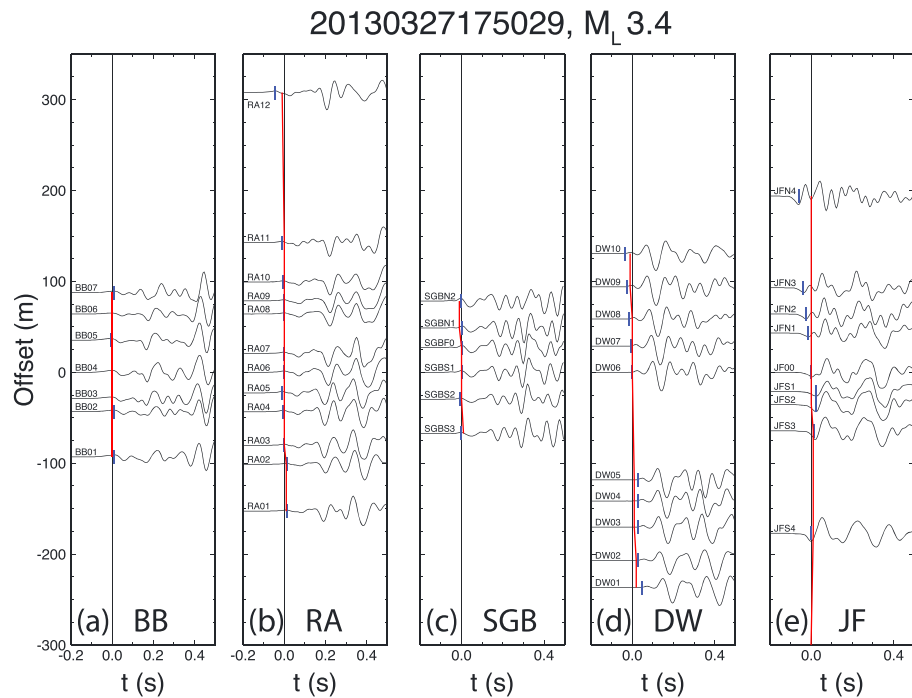


Figure 3. Initial P waves of an M_L 3.4 earthquake recorded at all five arrays. Vertical components of waveforms of the event recorded at arrays (a) BB, (b) RA, (c) SGB, (d) DW, and (e) JF. The X axis is in the P wave time window relative to traveltimes at the reference station of each array. The Y axis is the offset from the reference station of each array from southwest to northeast. Blue vertical bars show the manually picked P wave arrivals. Red lines represent predicted traveltimes based on a 1-D velocity model.

at all stations of the BB array that are ~ 38 km away (Figure 3a). In comparison, there are slight delays across the RA array, ~ 27 km from the earthquake. P waves arrive first at the northeast most station RA12 and then travel to other RA stations at nearly identical times (Figure 3b). Note that the RA array is nearly twice as long as the BB array. If we only compare the P arrivals at a portion with the same length of the BB array, e.g., RA10-RA03, there appears to be no obvious delay. Similarly, we do not find clear delays across the SGB array (Figure 3c), which is nearly the same length as the BB array. The epicentral distances to the SGB array are ~ 14.5 km. In contrast, we find more prominent delays at the DW array, where the arrival time is the smallest at the northeastmost station DW10 and gradually increases from northeast to southwest (Figure 3d). The delays are still obvious even if we consider a portion of the array, e.g., DW10-DW06, in a comparable size to arrays BB and SGB. Note that the M_L 3.4 earthquake is ~ 4 km northeast to the array DW and is nearly along the array azimuth (Figure 2d). The geometrical effects of the array (i.e., different epicentral distances among stations) are larger than those at other arrays further away. Among the five arrays, the most prominent delays of P waves for this event are observed at the JF array. P waves arrive clearly earlier at the northeast stations than at the southwest stations (Figure 3e). Considering only stations from JFN3 to JFS3 with approximately the same length of arrays BB and SGB, we can still find clear arrival time delays. The epicentral distances to the JF stations are ~ 8.9 km and the event-array direction is nearly perpendicular to the array azimuth (Figure 2e), suggesting less geometrical effects than that of the DW array.

We quantify the across-array delays of direct P waves by calculating traveltimes differences, d_{tp} , between the northeasternmost and southwesternmost stations of the arrays. If d_{tp} is positive, P waves arrive at the southwest stations earlier than at the northeast stations. Figure 4 shows the distributions of d_{tp} for all five arrays relative to distances normal to the strike of the SJFZ. The distributions can be divided into two groups: one with both positive and negative d_{tp} , such as at arrays RA, SGB, and JF, and another with only positive (BB) or negative (DW) d_{tp} . A pattern with positive-and-negative d_{tp} values can be used to estimate the dip angle of LVZ and to verify the catalog earthquake locations [e.g., Yang and Zhu, 2010]. Despite the difference in array lengths and locations, the d_{tp} distributions at arrays RA, SGB, and JF

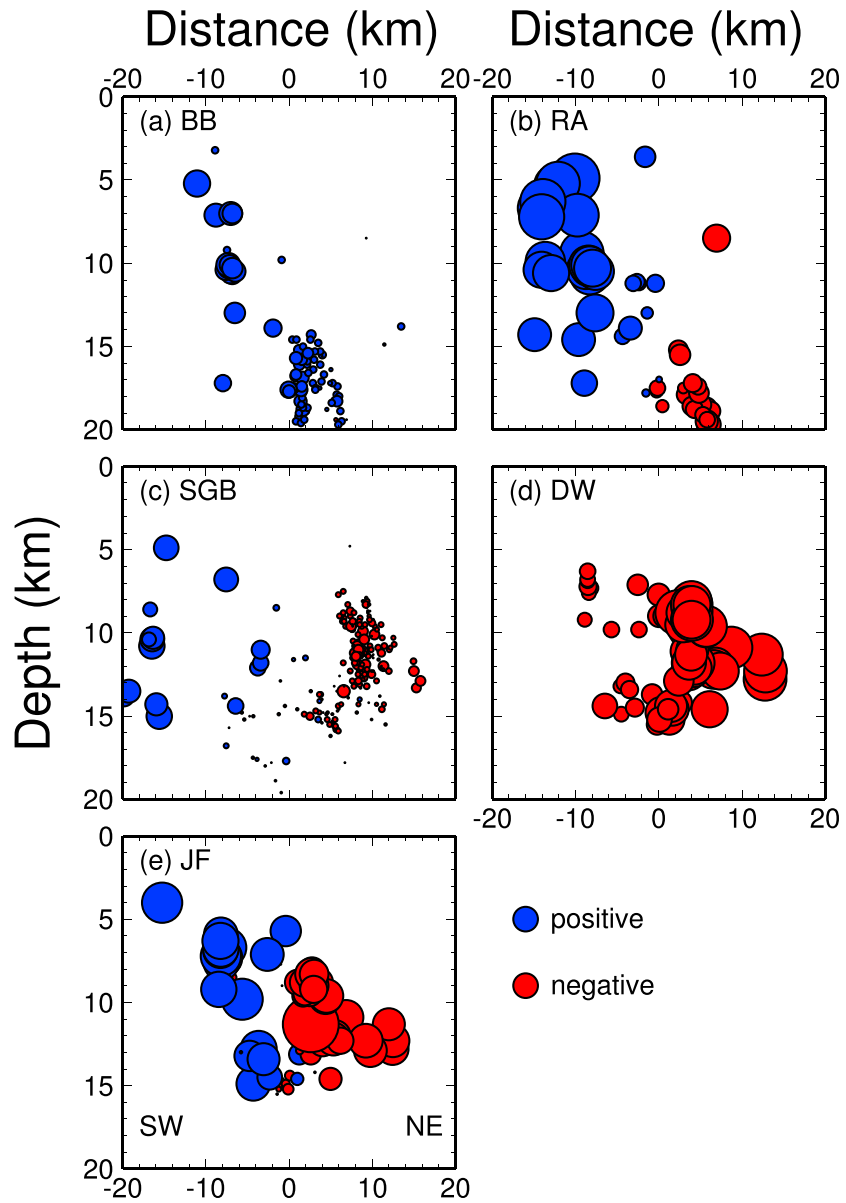


Figure 4. Cross sections of microearthquakes beneath each array. The circle sizes correspond to the differential times of *P* waves between the northeastmost and southwestmost stations of the across-fault arrays. Blue represents positive differential times; i.e., *P* waves arrive at the southwest stations earlier than at the northeast stations. *X* axis is distance relative to the center station normal to the strike of the SJFZ with northeast in the positive direction. Map view of these event locations is in Figure 2.

suggest a nearly vertical FZ (Figures 4b, 4c, and 4e). In contrast, the dtp distributions at arrays BB and DW show that the *P* waves always arrive faster at stations on one side than the other (Figures 4a and 4d). Furthermore, the amplitudes of the dtp are significantly larger at one side than the other, i.e., southwest to the array BB and northeast to the array DW (Figures 4a and 4d). Assuming a vertical FZ and reliable earthquake locations, the observations at arrays BB and DW suggest strong local heterogeneous velocity structures, such as bimaterial contrast or/and LVZ beneath these arrays.

Given that different epicentral distances could also lead to such across-array delays, we examine the traveltimes residuals between observed and theoretical *P* wave traveltimes predicted from an average 1-D velocity model [Allam and Ben-Zion, 2012]. If the across-array delays are primarily caused by differences in

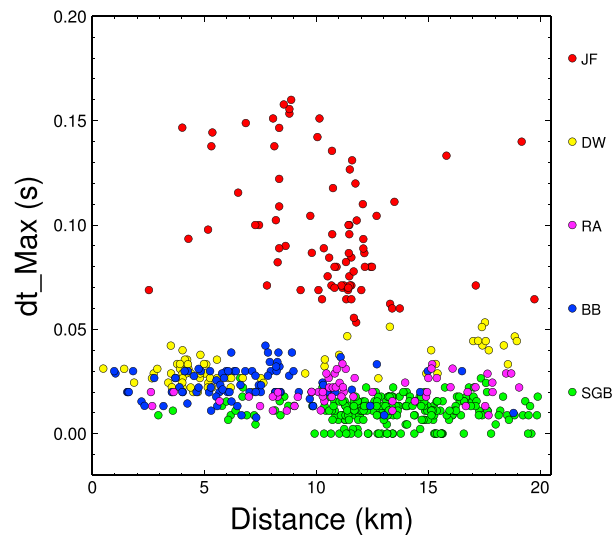


Figure 5. Maximum differential times across the entire array between predicted and observed P wave arrivals. Colors represent arrays BB (blue), RA (purple), SGB (green), DW (yellow), and JF (red), respectively.

epicentral distances, the predicted traveltimes should generally match the observations; i.e., the traveltime residuals between observations and predictions should be zero or very small. Predicted traveltimes for P waves of the M _{3.4} earthquake have subtle delays across all the arrays (Figure 3). Compared to the predictions, observed arrival times at array DW show slight advance in the northwest stations and delay in the southwest stations (Figure 3d). For the JF array, the manually picked arrival times deviate even more from the predictions compared to the DW array. The largest difference is approximately 0.1 s at station JFN4 (Figure 3e). In contrast, there is negligible difference between predicted and observed P wave arrivals across arrays BB and SGB. We quantify the differences by calculating the maximum differential times of observed and predicted P arrivals. In order to better show the variations in maximum differential times among the five arrays, we use their absolute values. The maximum differential times appear to be independent of epicentral distances but vary between the arrays (Figure 5). For instance, the maximum differential times of all events recorded at SGB array (green in Figure 5) are relatively small, while the observed P arrivals at the JF array (red in Figure 5) significantly deviate from predictions. The patterns of maximum differential times between observations and predictions among all five arrays indicate that there are clear along-strike variations of the internal FZ structures in this region.

3.2. Width and Velocity Reduction of Damage Zones

To further quantify FZ parameters, we compute synthetic waveforms of body waves transmitted through a LVZ and reflected from its boundaries [Li *et al.*, 2007]. From the above analysis of across-array time delays, we infer that the FZ beneath the arrays RA, SGB, and JF is near vertical. We cannot completely rule out that the LVZ is not vertical beneath arrays BB and DW, but recent tomography results suggest the LVZ is nearly vertical at these locations [Allam *et al.*, 2014]. Using earthquake and station locations (including station elevations) as well as the strike of the surface fault trace (126° clockwise from north), we rotate the three-component seismograms into the FZ radial, FZ normal, and FZ parallel directions (see details in Li *et al.* [2007]). We then compute synthetic waveforms using a method based on the Generalized Ray Theory (GRT) [Helmberger, 1983], which allows us to trace individual seismic rays bouncing from the LVZ boundaries. Compared with modeling of trapped waves [e.g., Peng *et al.*, 2003; Lewis *et al.*, 2005], this technique can reduce the trade-off between the LVZ width and velocities [e.g., Li *et al.*, 2007; Yang and Zhu, 2010].

Figure 6 shows a waveform record section at array RA from an earthquake (SCEC catalog ID: 15239473, local magnitude M _l 1.61) located on the southwestern side of the SJFZ near the Anza seismic gap. Both the P and S waves arrive first at the southwestmost station, RA01. Then the direct P and S wave arrivals are increasingly delayed, and the delay ends near station RA07 (Figure 6). The increase in delays occurs over a distance of ~200 m, which corresponds approximately to the LVZ width obtained below. In comparison, Figure 7 shows another waveform record section at array RA from an event (SCEC catalog ID: 15242089, local magnitude 1.80) located on the northeastern side of the SJFZ. Both P and S waves arrive first at the northeastmost station, RA12. The arrival time delays of the direct P and S waves start from northeast, near station RA07 (Figure 7). Such delays of direct P and S waves across the RA array is ubiquitous for earthquakes on both sides of the fault, again indicating the existence of a LVZ along the Anza segment. However, the LVZ may not be completely covered by the RA array; i.e., the southwest boundary of the LVZ may lie farther to the southwest of station RA01 (Figures 6 and 7).

20121101090424

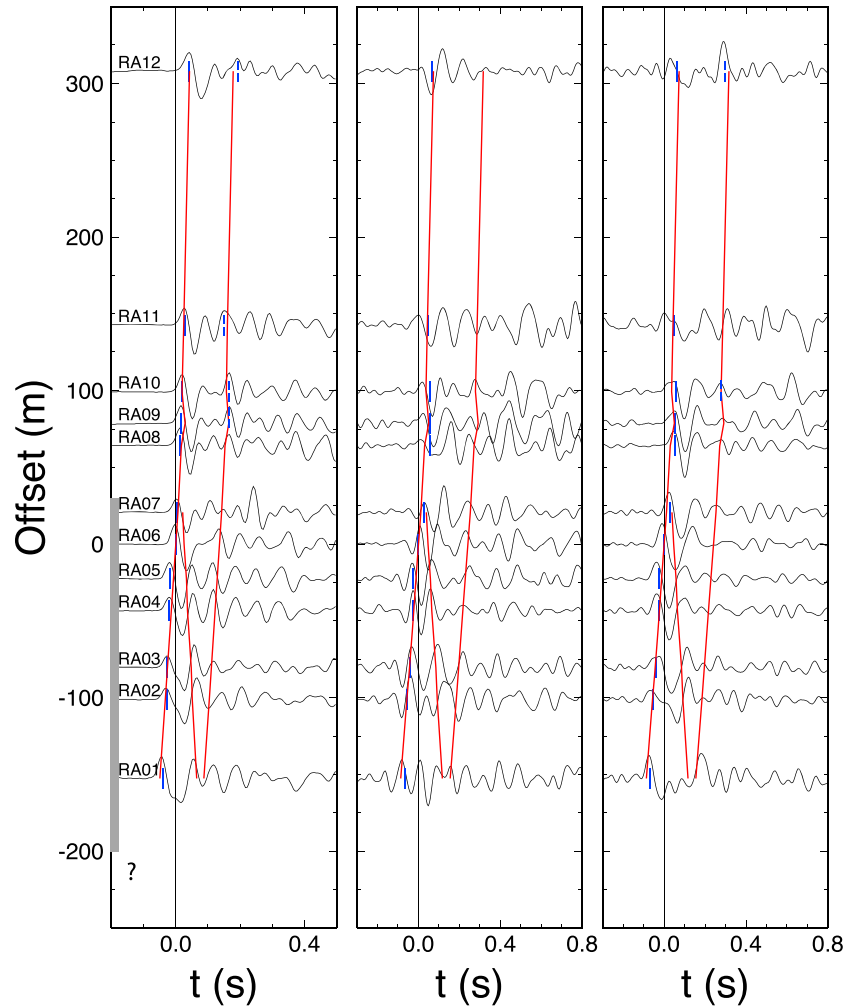


Figure 6. (left) Vertical, (middle) radial, and (right) tangential components of waveforms from an M_l 1.61 earthquake (SCEC ID: 15239473) recorded at the RA array (azimuth 43°). Epicentral distance and back azimuth of the earthquake are ~ 16 km and $\sim 261^\circ$, respectively. The vertical component is in the P time window and the radial and tangential components are in the S window. The Y axis is the offset from the central station of the RA array from southwest to northeast. Manually picked first (solid) and FZ-reflected (dashed) arrivals are marked by blue vertical bars. Red lines represent the direct and FZ-reflected P and S arrivals computed from a 1-D vertical LVZ model (width and velocity drop obtained in this study). Grey bar marks the approximate extent of the LVZ.

Following previous studies [Li et al., 2007; Yang and Zhu, 2010], we compute theoretical arrival times of the direct and FZ-reflected waves using the GRT with a 1-D layered model. We consider a LVZ embedded in host rock, which is approximated by a half space. We fix the V_p and V_s values of the host rock to be 6.2 km/s and 3.6 km/s, respectively, which are close to the average velocities at 5 km depth in this region [Allam and Ben-Zion, 2012; Zigone et al., 2014a]. The Q value in the LVZ is set to be 20, similar to the results from inversions of fault zone trapped waves in this region [Lewis et al., 2005]. We then perform forward modeling to compare the predicted travel times of the direct waves with observations (Figures 6 and 7). According to our results from forward modeling, the best estimated reduction of both V_p and V_s in the FZ is 50% relative to the host rock. The width of the LVZ below the RA array is ~ 230 m.

Similarly, we also find evidence of LVZs below arrays JF and DW based on travel time delays of first P and S arrivals. Figure 8 shows a waveform cross section recorded at the JF array for an example earthquake (SCEC ID: 11063837, local magnitude 2.58). Arrival time delays start from southwest between stations JF54

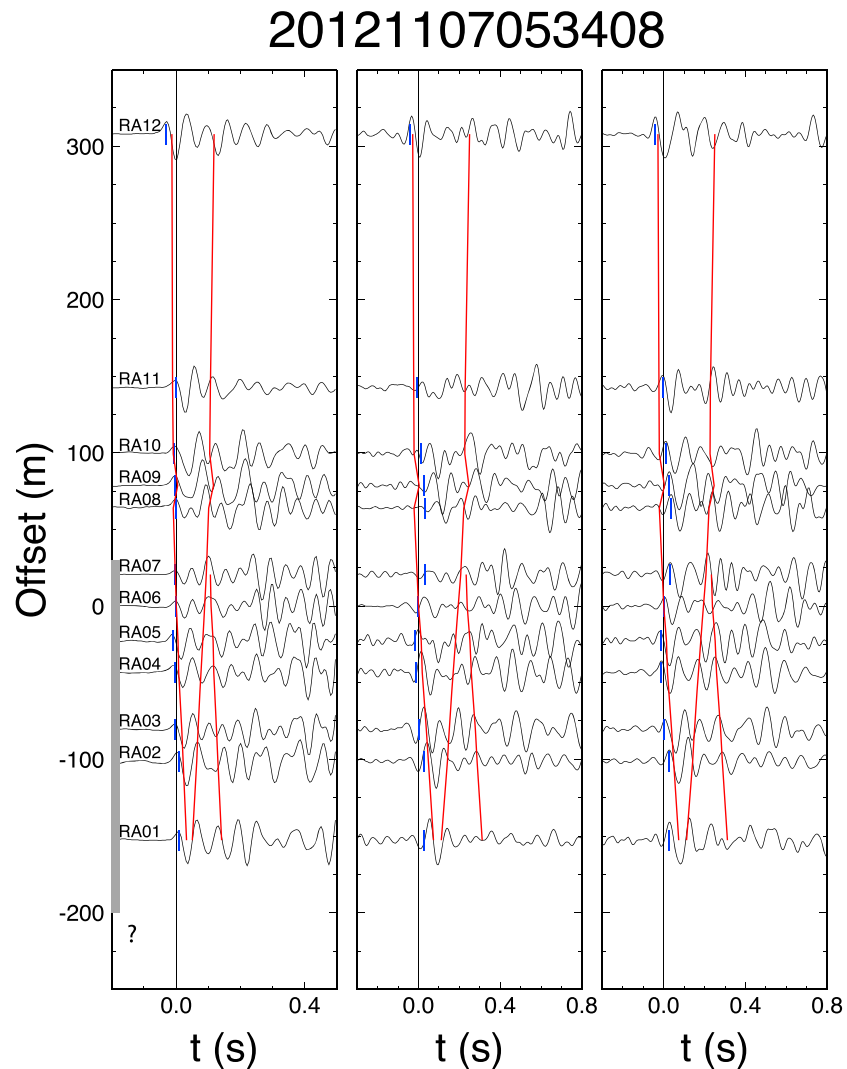


Figure 7. Vertical, radial, and tangential components of waveforms from an M_l 1.8 earthquake (SCEC ID: 15242089) recorded at the RA array. Epicentral distance and back azimuth are ~ 8 km and $\sim 350^\circ$, respectively. Other symbols and notations are the same as Figure 6, except that the earthquake is in the northeastern side of the SJFZ.

and JFS3 for both P and S waves. Our forward modeling indicates that the LVZ is approximately 200 m wide and the velocity reduction is $\sim 45\%$ in V_p and $\sim 55\%$ in V_s . At array DW, the LVZ-induced arrival time delays appear to start from the southwest between stations DW05 and DW06 and gradually extend to station DW10 and probably farther northeast (Figure 9). From the forward modeling, we estimate that the LVZ has a width of 200 m and velocity reductions of 30% in V_p and 50% in V_s . Since the LVZ may not be completely covered by the DW array, there could be strong trade-off between the LVZ width and velocity reduction.

Compared to arrays RA, JF, and DW, we do not find consistent gradual delays of arrival times of the direct P waves across the BB and SGB arrays (e.g., Figures 3a and 3c). Although there are across-array delays of direct P waves if we only consider the two end stations (Figures 4a and 4c), such delays only occur at one or two stations, making it difficult to quantify the width and velocities of the LVZs if they exist. For instance, the arrival times of P and S waves for an earthquake (SCEC ID: 15274633, local magnitude 1.39) only show considerable delays at stations BB06 and BB07 (Figure 10). While it is possible that such delays are caused by LVZs, they are not well sampled by arrays BB and SGB due to their smaller apertures.

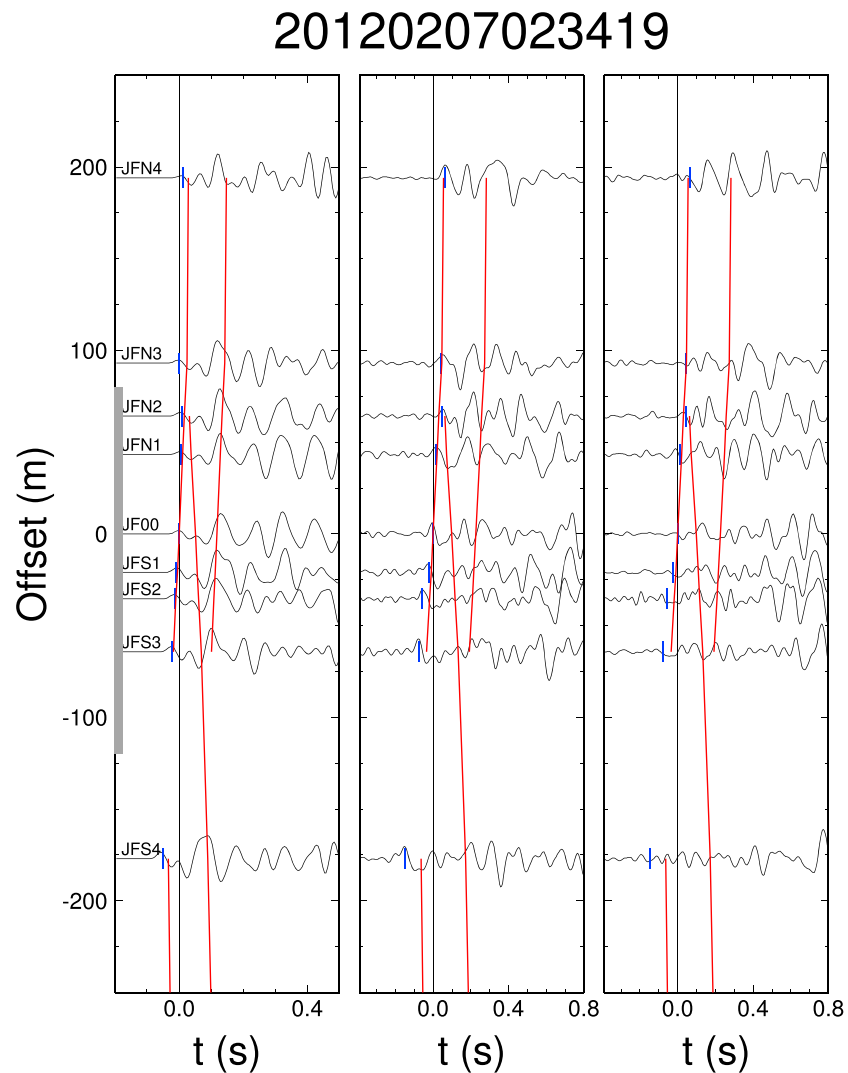


Figure 8. Vertical, radial, and tangential components of waveforms from an M_f 2.58 earthquake (SCEC ID: 11063837) recorded at the JF array (azimuth 45°). Epicentral distance and back azimuth are ~ 6.9 km and $\sim 167^\circ$, respectively.

3.3. Trade-Off Between Width and Velocity Reduction of LVZs

In addition to observing the arrival time delays of the direct P and S waves, we try to identify clear FZ-reflected P and S waves [Li *et al.*, 2007]. Although we could mark the FZ-reflected phases among a few stations (e.g., Figure 6), we do not observe coherent FZ-reflected P and S waves across the entire arrays (Figures 7–9). Since the differential arrival times between the direct and FZ-reflected P and S phases provide additional constraints on the width and velocity of the LVZ, our forward modeling results based on the first arrivals alone may have considerable trade-off between the width and velocity due to the lack of coherent FZ-reflected phases.

In order to estimate the potential trade-off, we perform a grid search of the best width and velocity of the LVZ by computing traveltime residual between the predicted and observed arrivals [e.g., Yang and Zhu, 2010]. The grid in width is set to be 10 m, and the search range is from 50 m to 350 m. The velocity reduction relative to the host rock is searched in every 2.5% from 10 to 80%. All direct and available FZ-reflected P and S arrivals are used in the grid search process (Table S2). After performing the grid search for each individual event, we obtain the overall traveltime residuals for an array by summing individual residual of each event.

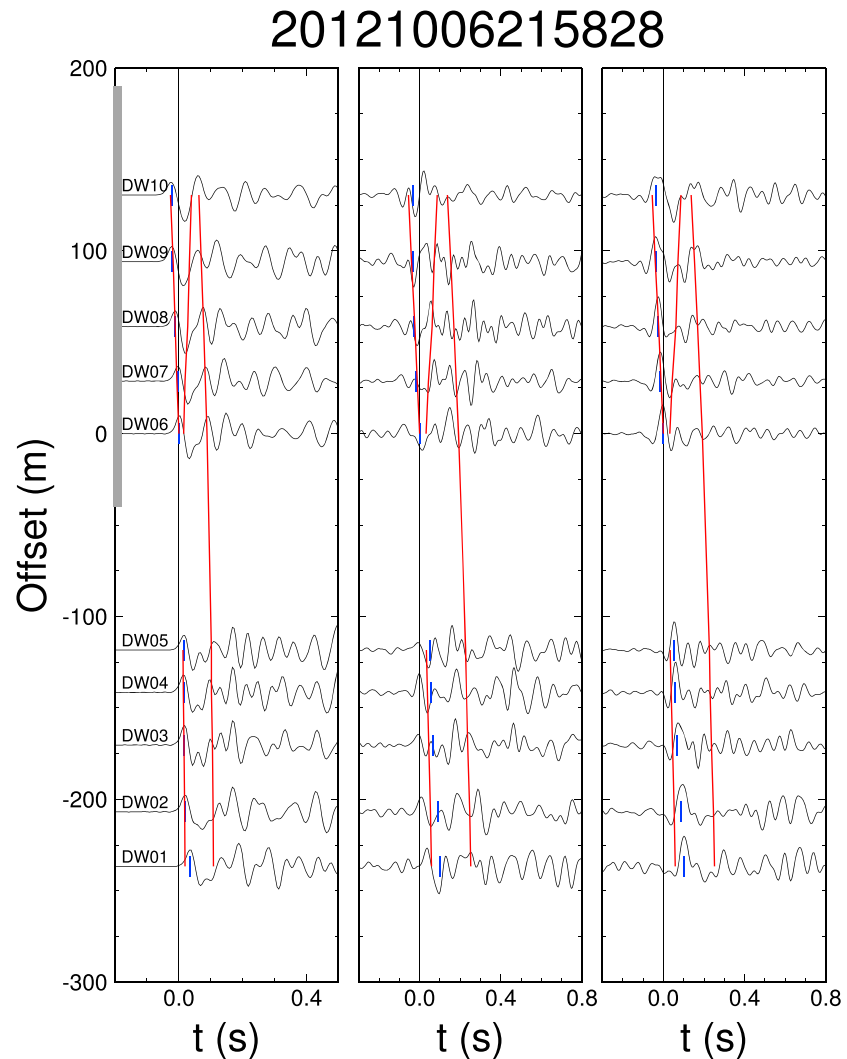


Figure 9. Vertical, radial, and tangential components of waveforms from an M 2.15 earthquake (SCEC ID: 15225769) recorded at the DW array (azimuth 40). Epicentral distance and back azimuth are ~ 7.5 km and $\sim 97^\circ$, respectively.

Figure 11 shows the overall traveltime residuals computed for arrays JF and RA. The best determined width at the JF array is ~ 150 – 200 m corresponding to a velocity reduction of 50–65%. Note that the upper limit of the LVZ width is well constrained to be ~ 200 m, but the lower limit of the LVZ width has larger uncertainties. This is related to the station spacing and the lack of coherent FZ-reflected phases as mentioned before. For example, the southwestern boundary of the LVZ at the JF array is between stations JFS4 and JFS3 (Figure 8), which are nearly 100 m apart and thus result in considerable uncertainties of the LVZ width. In contrast, the northeastern boundary is well bounded by stations JFN2 and JFN3 (Figure 8) that are only 25 m apart. Therefore, the uncertainties of the LVZ width are largely from the uncertainties of the southwestern boundaries, which in turn lead to considerable trade-off between the width and velocity reduction of the LVZ. Such trade-off is even larger at arrays RA and DW, where at least one side of the LVZ may be located beyond the coverage of the array. For instance, if we sum the arrival time residuals for 20 events (Table S2) of the RA array, we still find considerable trade-off between the width and the velocity reduction relative to the host rock. The width of the LVZ is bounded between 140 and 260 m, and the velocity reduction ranges from $\sim 50\%$ to $\sim 65\%$. It is worth noting that our forward modeling results agree well with the grid search-determined best solution (Figure 11).

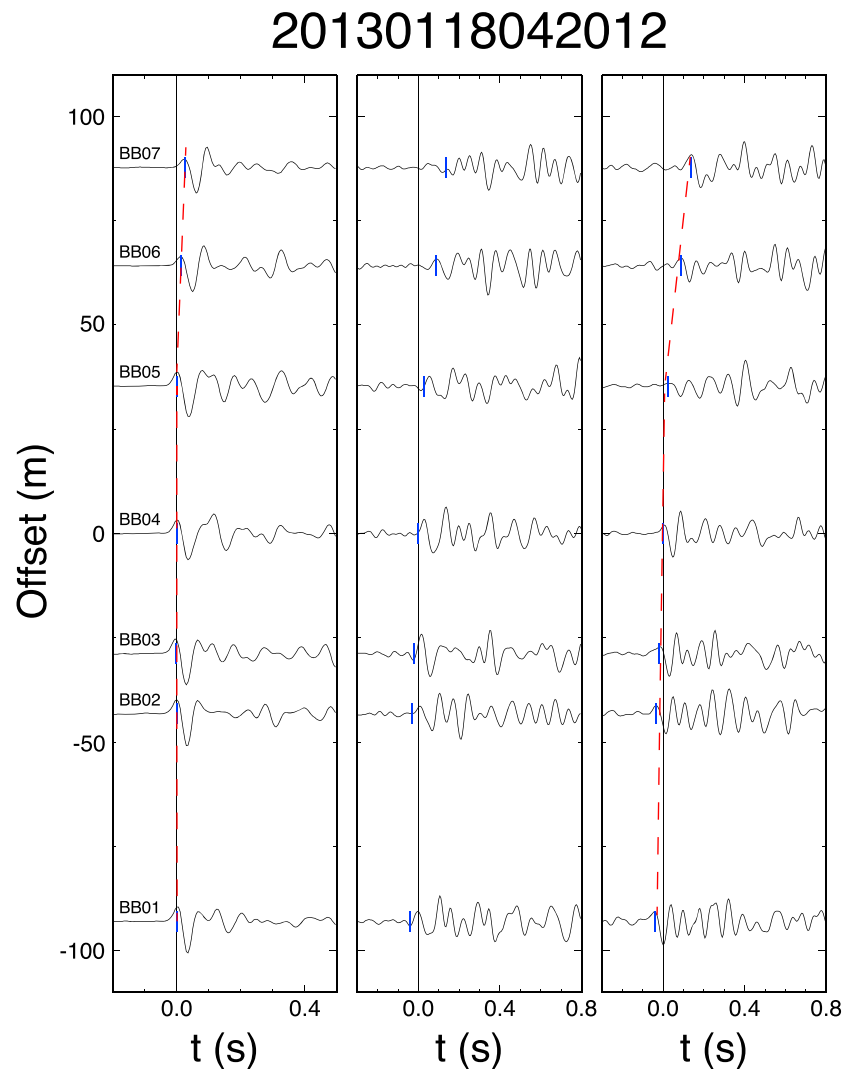


Figure 10. Vertical, radial, and tangential components of waveforms from an M_l 1.39 earthquake (SCEC ID: 15274633) recorded at the BB array (azimuth 45). Epicentral distance and back azimuth are ~ 1.0 km and $\sim 86^\circ$, respectively. Dashed red lines represent the trends of P and S arrivals.

4. Discussion and Conclusions

We determine the properties of internal LVZs along several sections of the SJFZ by modeling traveltimes of P and S waves of local earthquakes recorded at newly deployed small-aperture arrays. Out of the five small-aperture arrays, we found well-developed LVZs at arrays RA, DW, and JF. The widths of the LVZs are ~ 200 m, and the velocity reductions relative to the host rock are ~ 30 – 50% in V_p and ~ 50 – 60% in V_s . These findings are consistent with previous results from the data set recorded at temporary seismic experiments (1995 and 1999), in which three small-aperture arrays were deployed across different branches of the SJFZ, respectively [Li *et al.*, 1997; Li and Vernon, 2001; Lewis *et al.*, 2005]. In particular, one array across the Clark Fault (CF) was deployed in 1999 and was located approximately 1 km southeast to the JF array, sampling nearby segment of the SJFZ (Figure 1). According to analysis of FZ-trapped waves and body waves from the 1999 experiment, the LVZ associated with the CF was estimated to be ~ 200 m in width and had $\sim 50\%$ reduction in V_s and $\sim 40\%$ reduction in V_p [Li and Vernon, 2001; Lewis *et al.*, 2005; Yang and Zhu, 2010], nearly identical to what was reported for the JF array in this study.

The results complement recent larger-scale tomographic imaging of the SJFZ area based on earthquake and noise data with nominal horizontal resolution > 1 km. Allam and Ben-Zion [2012] and Allam *et al.* [2014]

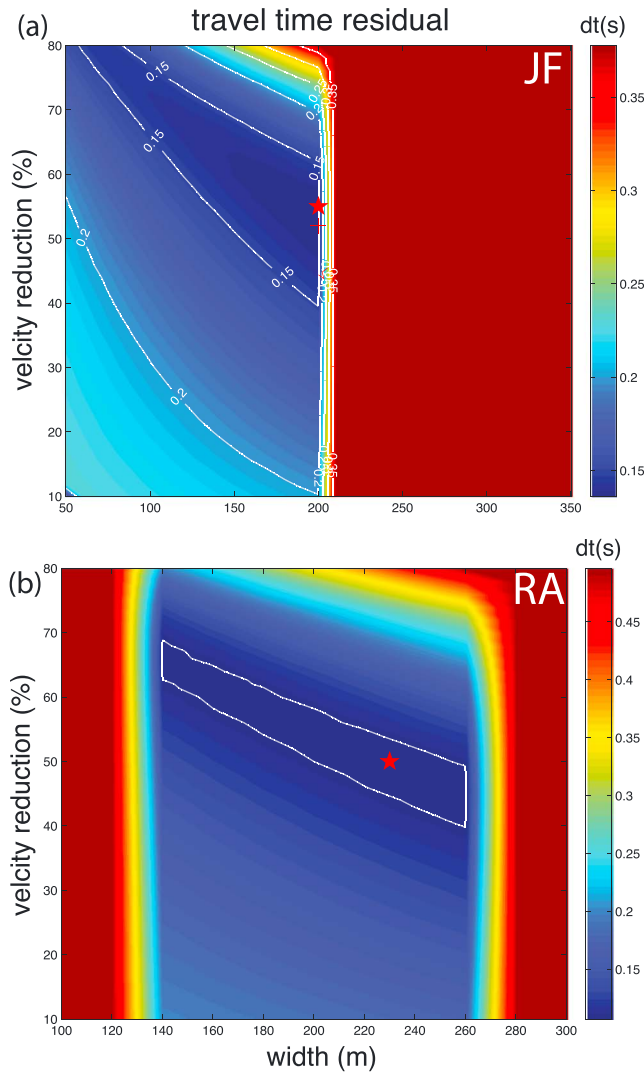


Figure 11. Overall traveltimes residuals (seconds) for different width and velocity reduction relative to the host rock for arrays (a) JF and (b) RA. Star denotes the initial estimate from the forward modeling.

observed with double-difference earthquake tomography several kilometers wide LVZs along the SJFZ that are especially pronounced in the top 5 km and show clean variations along the fault strike. *Zigone et al. [2014a]* obtained similar results on LVZs along the SJFZ from tomography based on the ambient seismic noise at frequencies up to 1 Hz. Recent analyses of noise at frequencies of several tens of Hz [*Zigone et al., 2014b*] and fault zone head and trapped waves [*Qiu et al., 2014; Share et al., 2014*] recorded by the same linear arrays we used (Figure 1) reveal inner damage zones with width and velocity reductions similar to those obtained in this work.

The fault zone arrays were deployed to cross the known main traces of the SJFZ at different locations. The derived results on the internal fault zone structure may be affected by local basins and sedimentary layers near the fault zone. Using the current data set, we cannot rule out that the across-array delays are partly caused by local sediment-filled basins. However, such local sedimentary layers are created by, and form part of, the shallow fault zone structure. Based on a detailed study associated with the North Anatolian Fault, *Ben-Zion et al. [2003]* suggested that shallow trapping structures include fault zone-related basins and that the anomalous motion in these zones may be referred to generally as fault

zone-related site effects. These designations are likely also relevant for the SJFZ and other fault zone structures.

Out of the five temporary arrays, we only find prominent LVZs at arrays RA, DW, and JF. Furthermore, the velocity reduction at the DW array is smaller than those at arrays RA and JF. The lack of observed LVZs below the SGB and BB arrays is probably related to their short aperture and location with respect to inner damage zones at these locations. Our results document clear along-strike variations of the internal fault zone structure of the SJFZ. This is consistent with the larger-scale variations seen in the regional tomographic studies in the area [*Allam and Ben-Zion, 2012; Allam et al., 2014; Zigone et al., 2014a*], and along-strike variations of trapping structures observed in the context of the Landers rupture zone [*Peng et al., 2003*] and the Parkfield section of the San Andreas Fault [*Lewis and Ben-Zion, 2010*]. Such along-strike heterogeneity in fault damage may play a significant role in rupture propagation and termination, and the exact effects could be investigated by running numerical experiments on dynamic rupture simulations.

We attempt to estimate the depth extent of the imaged LVZs by tracking the raypaths transmitted through the LVZs. This is illustrated in Figure 12 with a cross section of generalized rays traveling from an earthquake (SCEC ID: 15226721, local magnitude 1.07) to the RA array. Due to the source-receiver geometry, the seismic rays sample the FZ at depths of less than 2 km. We also consider a few factors

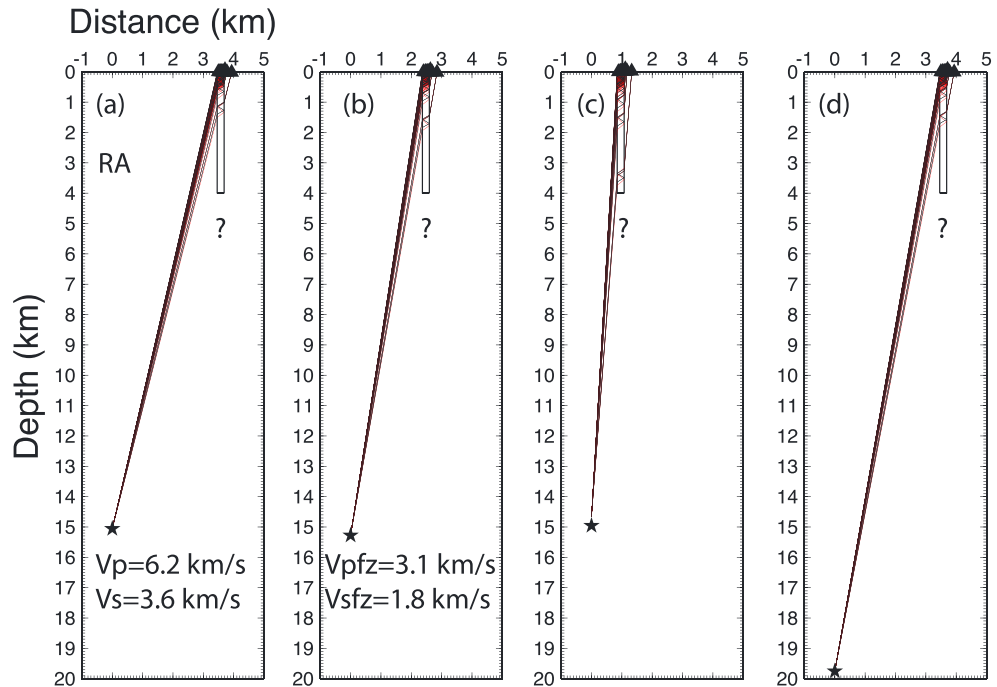


Figure 12. An example of seismic rays from an earthquake (SCEC ID: 15226721, local magnitude 1.07) (star) to RA stations (triangle), traveling through a tabular low-velocity zone (rectangle). V_p and V_s denote the P and S wave velocities in the host rock, and V_{pfz} and V_{sfz} represent those in the LVZ. (a) No perturbation, (b) 10° perturbation on back azimuth, (c) 5 km perturbation on epicentral distance, and (d) 5 km perturbation on event depth.

that may lead to uncertainties of the sampling depths, such as earthquake locations. We find that the uncertainties are generally no more than 1.5 km given 5 km perturbations on event epicentral distance and focal depth (Figure 12). We also apply a 10° perturbation on the back azimuth and find the resulting uncertainties are approximately 1 km (Figure 12). We inspect all earthquakes sampling the LVZs beneath the JF, RA, and DW arrays and find that the sampling depths are no more than 4 km. While these results suggest relatively shallow inner LVZs, we cannot rule out the possibility that the LVZs extend to greater depths not sampled by the utilized body waves. Data recorded by longer arrays across the fault can provide stronger constraints on the depth of the LVZs with the current method [Yang et al., 2011]. Recent inversions of trapped waves at stations of the JF array suggest that the inner LVZ at that location extends to a depth of 3–5 km [Qiu et al., 2014]. These results agree with the previous findings of Lewis et al. [2005] and Yang and Zhu [2010] at nearby locations along the SJFZ, and with simulation results on decreasing damage with depth [Ben-Zion and Shi, 2005; Finzi et al., 2009; Kaneko and Fialko, 2011].

According to our across-array traveltimes analysis and previous tomographic results [Allam et al., 2014], we infer that the LVZ is nearly vertical in the 50 km along-strike distance. However, the LVZs might not be perfectly vertical according to previous studies [e.g., Yang and Zhu, 2010; Yang et al., 2011]. A dipping fault zone layer may have little effects on determining the LVZ width and velocity reduction given the consistently observed direct and FZ-reflected waves [Li et al., 2007]. However, there might be considerable trade-off between the LVZ depth extent and the dip. Such uncertainties can be overcome by modeling depth-sensitive waveforms or travel time pattern from both sides of the LVZ, using longer aperture arrays, as shown in previous studies [e.g., Yang and Zhu, 2010; Yang et al., 2011].

Prominent FZ-reflected P and S waves were observed at a linear array across the Landers fault shortly after the 1992 M_w 7.3 Landers earthquake [Li et al., 2007]. However, such clear FZ-reflected phases are not identified coherently on the cross-fault arrays in this study and were also not observed along the SJFZ in data of the earlier 1999 experiment [Yang and Zhu, 2010]. The differences may stem from both physical and observational factors. Since the array across the Landers fault was deployed shortly after the

M_w 7.3 earthquake, the velocity contrast between the damage zone and the host rock may have formed sharp boundaries that can generate clear FZ-reflected waves. In contrast, the SJFZ has not experienced major ruptures in over 100 years, and therefore, the LVZ boundaries might be gradual, resulting in less prominent reflected phases. In addition, the aperture of the array across the Landers fault is nearly ~ 1.5 km, approximately 3 times as long as the arrays used in this study. The limited number of stations (~ 10) within each array makes it more challenging to track the FZ-reflected phases. Indeed, we have marked the FZ-reflected P and S waves at a few stations (Figure 6), but these phases are not coherently observed across the entire array. A dense array with a larger aperture, such as the experiment across the Landers [Li *et al.*, 2007] and Calico faults [Cochran *et al.*, 2009; Yang *et al.*, 2011] provide better opportunities to observe more coherent high-frequency FZ-related phases and resolve the FZ structure with higher resolution.

The Anza seismic gap has not experienced any surface-rupturing earthquakes for at least 200 years [Salisbury *et al.*, 2012]. Our observations of LVZ in that region and other sections of the SJFZ indicate that parts of the damage structure of faults remain throughout (and beyond) large earthquake cycles. This is consistent with the observations of Rovelli *et al.* [2002] of damaged fault zone layer in a dormant fault in Nocera Umbra in Italy, the observations of Cochran *et al.* [2009], Yang *et al.* [2011] and Hillers *et al.* [2014] on trapping structures along the Calico fault, and observations on very slow healing process of coseismic velocity changes at various locations at least at shallow depths [e.g., Peng and Ben-Zion, 2006; Liu *et al.*, 2014].

Acknowledgments

This work was supported by the National Science Foundation under grant EAR-0908310 (H.Y., Z.L., and Z.P.), grant EAR-0908903 (Y.B.Z.), and grant EAR-0908042 (F.L.V.). We thank the Associated Editor and anonymous referees for useful comments. H.Y. benefitted from discussions with Lupei Zhu at Saint Louis University. The figures are made from Generic Mapping Tools (GMT) and MATLAB. Seismic waveform data are obtained from Data Management Center (DMC) of Incorporated Research Institutions for Seismology (IRIS), <http://www.iris.edu/hq/>.

References

- Allam, A. A., and Y. Ben-Zion (2012), Seismic velocity structures in the southern California plate-boundary environment from double-difference tomography, *Geophys. J. Int.*, *190*, 1181–1196.
- Allam, A. A., Y. Ben-Zion, I. Kurzon, and F. Vernon (2014), Seismic velocity structure in the Hot Springs and trifurcation areas of the San Jacinto Fault Zone, California, from double-difference tomography, *Geophys. J. Int.*, *198*(2), 978–999, doi:10.1093/gji/ggu176.
- Avallone, A., A. Rovelli, G. Di Giulio, L. Improta, Y. Ben-Zion, G. Milana, and F. Cara (2014), Wave-guide effects in very high rate GPS record of the 6 April 2009, M_w 6.1 LAquila, central Italy earthquake, *J. Geophys. Res. Solid Earth*, *119*, 490–501, doi:10.1002/2013JB010475.
- Ben-Zion, Y., and J.-P. Ampuero (2009), Seismic radiation from regions sustaining material damage, *Geophys. J. Int.*, *178*(3), 1351–1356, doi:10.1111/j.1365-246X.2009.04285.x.
- Ben-Zion, Y., and Y. Huang (2002), Dynamic rupture on an interface between a compliant fault zone layer and a stiffer surrounding solid, *J. Geophys. Res.*, *107*(B2), 2042, doi:10.1029/2001JB000254.
- Ben-Zion, Y., and C. G. Sammis (2003), Characterization of fault zones, *Pure Appl. Geophys.*, *160*, 677–715.
- Ben-Zion, Y., and Z. Shi (2005), Dynamic rupture on a material interface with spontaneous generation of plastic strain in the bulk, *Earth Planet. Sci. Lett.*, *236*, 486–496, doi:10.1016/j.epsl.2005.03.025.
- Ben-Zion, Y., Z. Peng, D. Okaya, L. Seeber, J. G. Armbruster, N. Ozer, A. J. Michael, S. Baris, and M. Aktar (2003), A shallow fault-zone structure illuminated by trapped waves in the Karadere-Duzce branch of the North Anatolian Fault, western Turkey, *Geophys. J. Int.*, *152*(3), 699–717.
- Blisniuk, K., M. Oskin, A.-S. Meriaux, T. Rockwell, R. C. Finkel, and F. J. Ryerson (2013), Stable, rapid rate of slip since inception of the San Jacinto Fault, California, *Geophys. Res. Lett.*, *40*, 4209–4213, doi:10.1002/grl.50819.
- Chester, F. M., J. P. Evans, and R. L. Biegel (1993), Internal structure and weakening mechanisms of the San Andreas Fault, *J. Geophys. Res.*, *98*, 771–786, doi:10.1029/92JB01866.
- Cochran, E. S., Y. Li, P. M. Shearer, S. Barbot, Y. Fialko, and J. E. Vidale (2009), Seismic and geodetic evidence for extensive, long-lived fault damage zones, *Geology*, *37*, 315–318.
- Dor, O., T. K. Rockwell, and Y. Ben-Zion (2006), Geologic observations of damage asymmetry in the structure of the San Jacinto, San Andreas and Punchbowl faults in southern California: A possible indicator for preferred rupture propagation direction, *Pure Appl. Geophys.*, *163*, 301–349, doi:10.1007/s00024-005-0023-9.
- Fialko, Y. (2006), Interseismic strain accumulation and the earthquake potential on the southern San Andreas Fault System, *Nature*, *441*, 968–971.
- Fialko, Y., D. Sandwell, D. Agnew, M. Simons, P. Shearer, and B. Minster (2002), Deformation on nearby faults induced by the 1999 Hector Mine earthquake, *Science*, *297*, 1858–1862.
- Finzi, Y., E. H. Hearn, Y. Ben-Zion, and V. Lyakhovskiy (2009), Structural properties and deformation patterns of evolving strike-slip faults: Numerical simulations incorporating damage rheology, *Pure Appl. Geophys.*, *166*, 1537–1573, doi:10.1007/s00024-009-0522-1.
- Harris, R. A., and S. M. Day (1997), Effects of a low-velocity zone on a dynamic rupture, *Bull. Seismol. Soc. Am.*, *87*, 1267–1280.
- Helmberger, D. V. (1983), Theory and application of synthetic seismograms, in *Earthquakes: Observation, Theory and Interpretation*, pp. 174–222, Soc. Italiana di Fisica, Bologna, Italy.
- Hillers, G., M. Campillo, Y. Ben-Zion, and P. Roux (2014), Seismic fault zone trapped noise, *J. Geophys. Res. Solid Earth*, *119*, 5786–5799, doi:10.1002/2014JB011217.
- Huang, Y., J. Ampuero, and D. V. Helmberger (2014), Earthquake ruptures modulated by waves in damaged fault zones, *J. Geophys. Res. Solid Earth*, *119*, 3133–3154, doi:10.1002/2013JB010724.
- Kaneko, Y., and Y. Fialko (2011), Shallow slip deficit due to large strike-slip earthquakes in dynamic rupture simulations with elasto-plastic off-fault response, *Geophys. J. Int.*, *186*, 1389–1403.
- Kaneko, Y., J. P. Ampuero, and N. Lapusta (2011), Spectral-element simulations of long-term fault slip: Effect of low-rigidity layers on earthquake-cycle dynamics, *J. Geophys. Res.*, *116*, B10313, doi:10.1029/2011JB008395.
- Kurzon, I., F. L. Vernon, Y. Ben-Zion, and G. Atkinson (2014), Ground motion prediction equations in the San Jacinto Fault Zone—Significant effects of rupture directivity and fault zone amplification, *Pure Appl. Geophys.*, *171*, 3045–3081, doi:10.1007/s00024-014-0855-2.
- Lewis, M., and Y. Ben-Zion (2010), Diversity of fault zone damage and trapping structures in the Parkfield section of the San Andreas Fault from comprehensive analysis of near fault seismograms, *Geophys. J. Int.*, *183*, 1579–1595.

- Lewis, M. A., Z. G. Peng, Y. Ben-Zion, and F. L. Vernon (2005), Shallow seismic trapping structure in the San Jacinto Fault Zone near Anza, California, *Geophys. J. Int.*, *162*, 867–881.
- Li, Y. G., and F. L. Vernon (2001), Characterization of the San Jacinto Fault Zone near Anza, California, by fault zone trapped waves, *J. Geophys. Res.*, *106*, 30,671–30,688, doi:10.1029/2000JB000107.
- Li, Y. G., P. G. Leary, K. Aki, and P. Malin (1990), Seismic trapped modes in the Oroville and San Andreas Fault Zones, *Science*, *249*, 763–766.
- Li, Y. G., F. L. Vernon, and K. Aki (1997), San Jacinto Fault-Zone guided waves: A discrimination for recently active fault strands near Anza, California, *J. Geophys. Res.*, *102*, 11,689–11,701, doi:10.1029/97JB01050.
- Li, H., L. Zhu, and H. Yang (2007), High-resolution structures of the Landers fault zone inferred from aftershock waveform data, *Geophys. J. Int.*, *171*, 1295–1307.
- Li, H., et al. (2013), Characteristics of the fault-related rocks, fault zones and the principal slip zone in the Wenchuan Earthquake Fault Scientific Drilling Project Hole-1 (WFSD-1), *Tectonophysics*, *584*, 23–42.
- Lindsey, E. O., V. J. Sahakian, Y. Fialko, Y. Bock, S. Barbot, and T. K. Rockwell (2014), Interseismic strain localization in the San Jacinto Fault Zone, *Pure Appl. Geophys.*, *171*, 2937–2954, doi:10.1007/s00024-013-0753-z.
- Liu, Z., J. Huang, Z. Peng, and J. Su (2014), Seismic velocity changes in the epicentral region of the 2008 Wenchuan earthquake measured from three-component ambient noise correlation techniques, *Geophys. Res. Lett.*, *41*, 37–42, doi:10.1002/2013GL058682.
- Lutz, A. T., R. J. Dorsey, B. A. Housen, and S. U. Janecke (2006), Stratigraphic record of Pleistocene faulting and basin evolution in the Borrego Badlands, San Jacinto Fault Zone, Southern California, *Geol. Soc. Am. Bull.*, *118*(11–12), 1377–1397.
- Peng, Z., and Y. Ben-Zion (2006), Temporal changes of shallow seismic velocity around the Karadere-Duzce branch of the North Anatolian Fault and strong ground motion, *Pure Appl. Geophys.*, *163*, 567–600, doi:10.1007/s00024-005-0034-6.
- Peng, Z., Y. Ben-Zion, A. J. Michael, and L. Zhu (2003), Quantitative analysis of seismic fault zone waves in the rupture zone of the Landers, 1992, California earthquake: Evidence for a shallow trapping structure, *Geophys. J. Int.*, *155*, 1021–1041.
- Qiu, H., Y. Ben-Zion, Z. E. Ross, P.-E. Share, and F. Vernon (2014), Internal structure of the San Jacinto fault zone at Jackass Flat from data recorded by a dense linear array, The SCEC Annual Meeting 2014, SCEC, Palm Springs, Calif., 7 Sept.
- Rockwell, T. K., and Y. Ben-Zion (2007), High localization of primary slip zones in large earthquakes from paleoseismic trenches: Observations and implications for earthquake physics, *J. Geophys. Res.*, *112*, B10304, doi:10.1029/2006JB004764.
- Rovelli, A., A. Caserta, F. Marra, and V. Ruggiero (2002), Can seismic waves be trapped inside an inactive fault zone? The case study of Nocera Umbra, central Italy, *Bull. Seismol. Soc. Am.*, *92*, 2217–2232.
- Salisbury, J. B., T. K. Rockwell, T. J. Middleton, and K. W. Hudnut (2012), LiDAR and field observations of slip distribution for the most recent surface ruptures along the central San Jacinto Fault, *Bull. Seismol. Soc. Am.*, *102*(2), 598–619.
- Sanders, C. O., and H. Kanamori (1984), A seismotectonic analysis of the Anza seismic gap, San Jacinto Fault Zone, southern California, *J. Geophys. Res.*, *89*, 5873–5890, doi:10.1029/JB089iB07p05873.
- Schaff, D. P., G. H. R. Bokelmann, G. C. Beroza, F. Waldhauser, and W. L. Ellsworth (2002), High resolution image of Calaveras Fault seismicity, *J. Geophys. Res.*, *107*, 2186, doi:10.1029/2001JB000633.
- Schulz, S. E., and J. P. Evans (1998), Spatial variability in microscopic deformation and composition of the Punchbowl fault, southern California: Implications for mechanisms, fluid-rock interaction, and fault morphology, *Tectonophysics*, *295*, 223–244.
- Share, P.-E., Y. Ben-Zion, Z. Ross, H. Qiu, and F. Vernon (2014), Characterization of the San Jacinto Fault Zone northwest of the trifurcation area from dense linear array data, The SCEC Annual Meeting 2014, SCEC, Palm Springs, Calif., 7 Sept.
- Smith, S. A. F., A. Bistacchi, T. M. Mitchell, S. Mittemperger, and G. D. Toro (2013), The structure of an exhumed intraplate seismogenic fault in crystalline basement, *Tectonophysics*, *599*, 29–44.
- Sykes, L., and S. Nishenko (1984), Probabilities of occurrence of large plate rupturing earthquakes for the San Andreas, San Jacinto and Imperial faults, California, *J. Geophys. Res.*, *89*(B7), 5905–5928, doi:10.1029/JB089iB07p05905.
- Thurber, C., H. Zhang, F. Waldhauser, J. Hardebeck, A. Micheal, and D. Eberhart-Phillips (2006), Three-dimensional compressional wavespeed model, earthquake relocations, and focal mechanisms for the Parkfield, California, region, *Bull. Seismol. Soc. Am.*, *96*(4B), S38–S49.
- Valoroso, L., L. Chiaraluce, and C. Colletini (2014), Earthquakes and fault zone structure, *Geology*, *42*(4), 343–346.
- Wechsler, N., T. K. Rockwell, and Y. Ben-Zion (2009), Application of high resolution DEM data to detect rock damage from geomorphic signals along the central San Jacinto Fault, *Geomorphology*, *113*, 82–96, doi:10.1016/j.geomorph.2009.06.007.
- Wu, C., Z. Peng, and Y. Ben-Zion (2009), Non-linearity and temporal changes of fault zone site response associated with strong ground motion, *Geophys. J. Int.*, *176*, 265–278.
- Xu, S., Y. Ben-Zion, and J.-P. Ampuero (2012), Properties of inelastic yielding zones generated by in-plane dynamic ruptures: II. Detailed parameter-space study, *Geophys. J. Int.*, *191*, 1343–1360, doi:10.1111/j.1365-246X.2012.05685.x.
- Yang, H., and L. Zhu (2010), Shallow low-velocity zone of the San Jacinto Fault from local earthquake waveform modelling, *Geophys. J. Int.*, *183*, 421–432.
- Yang, H., L. Zhu, and R. Chu (2009), Fault-plane determination of the 18 April 2008 Mt. Carmel, Illinois, earthquake by detecting and relocating aftershocks, *Bull. Seismol. Soc. Am.*, *99*(6), 3413–3420.
- Yang, H., L. Zhu, and E. S. Cochran (2011), Seismic structures of the Calico fault zone inferred from local earthquake travel time modelling, *Geophys. J. Int.*, *186*, 760–770.
- Zhang, J., and P. Gerstoft (2014), Local-scale cross-correlation of seismic noise from the calico fault experiment, *Earthquake Sci.*, *27*, 311–318, doi:10.1007/s11589-014-0074-z.
- Zigone, D., Y. Ben-Zion, M. Campillo, and P. Roux (2014a), Seismic tomography of the Southern California plate boundary region from noise-based Rayleigh and Love waves, *Pure Appl. Geophys.*, doi:10.1007/s00024-014-0872-1.
- Zigone, D., Y. Ben-Zion, M. Campillo, G. Hillers, P. Roux, and F. Vernon (2014b), Imaging the internal structure of the San Jacinto Fault Zone with high Frequency noise, The SCEC Annual Meeting 2014, SCEC, Palm Springs, Calif., 7 Sept.